EFFECT OF POLYDISPERSITY OF CLAY PLATELETS ON THE AGGREGATION AND MECHANICAL PROPERTIES OF CLAY AT THE MESOSCALE

Davoud Ebrahimi[1], Andrew J. Whittle[1], and Roland J.-M. Pellenq[1,2,3],*

[1] Department of Civil and Environmental Engineering, Massachusetts Institute of Technology, Cambridge, Massachusetts 02139, USA
[2] Centre Interdisciplinaire de Nanosciences de Marseille, Aix-Marseille Université, CNRS, Campus de Luminy, 13288 Marseille Cedex 09, France
[3] <MSE>[2], UMI 3466, CNRS-MIT, Cambridge, Massachusetts 02139, USA

Abstract—The results from mesoscale simulations of the formation and evolution of microstructure for assemblies of Na-smectite particles based on assumed size distributions of individual clay platelets are presented here. The analyses predicted particle arrangements and aggregation (*i.e.* platelets linked in face−face configurations) and are used to link geometric properties of the microstructure and mechanical properties of the particle assemblies. Interactions between individual ellipsoidal clay platelets are represented using the Gay-Berne potential based on atomistic simulations of the free energy between two Na-smectite clay-platelets in liquid water, following a novel coarse-graining method developed previously. The current study describes the geometric (aggregate thickness, orientation, and porosity) and elastic properties in the 'jammed states' from the mesoscale simulations for selected ranges of clay particle sizes and confining pressures. The thickness of clay aggregates for monodisperse assemblies increases (with average stack thickness consisting of $n = 3-8$ platelets) with the diameter of the individual clay platelets and with the level of confining pressure. Aggregates break down at high confining pressures ($50-300$ atm) due to slippage between the platelets. Polydisperse simulations generate smaller aggregates ($n = 2$) and show much smaller effects of confining pressure. All assemblies show increased order with confining pressure, implying more anisotropic microstructure. The mesoscale simulations are also in good agreement with macroscopic compression behavior measured in conventional 1-D laboratory compression tests. The mesoscale assemblies exhibit cubic symmetry in elastic properties. The results for larger platelets ($D = 1000$ Å) are in good agreement with nano-indentation measurements on natural clays and shale samples.

Key Words—Clay Aggregation, Mesoscale Simulation, Microstructure, Polydispersity, Potential of Mean Force.

INTRODUCTION

Particulate materials such as clay minerals have important applications in ceramics, oil-well drilling, rheology modifiers, waste disposal, and polymer composites (Murray, 1991). The size and shape of the particles affect the properties of the processed material (Adams, 1993). Platelets of clay are negatively charged due to isomorphous substitutions within the clay lattice; the clay adsorbs interlayer cations and becomes neutral. Long-range electrostatic Coulombic interactions and short-range van der Waals forces determine the stability of the system. Mean field approaches such as classical DLVO theory (Derjaguin *et al.*, 1941; Verwey and Overbeek, 1999) cannot capture short-range repulsion and structured layers of water molecules reported in experiments (Israelachvili and Pashley, 1983; Pashley and Israelachvili, 1984). Molecular dynamics is an alternative computational tool for studying material behavior by simulating interactions at the atomistic

scales enabling the study of nanoscale structural and mechanical properties of clay minerals as functions of water content (Heinz *et al.*, 2005; Boulet *et al.*, 2006; Suter *et al.*, 2007; Thyveetil *et al.*, 2007; Mazo *et al.*, 2008a, 2008b; Ebrahimi *et al.*, 2012; Carrier *et al.*, 2014), type of cation (Boek *et al.*, 1995; Young and Smith, 2000; Hensen *et al.*, 2001; Whitley and Smith, 2004; Li *et al.*, 2016), and surface charge (Zartman *et al.*, 2010) . Modeling the aggregation of clay platelets using full atomistic simulation (*i.e.* with atomistic interactions) requires a large model which is impractical even with recent advancements in computational power. Previous studies used quadrupoles (Dijkstra *et al.*, 1995) or pseudo (charge) sites (Kutter *et al.*, 2000; Jardat *et al.*, 2009; Sjoblom, 2015) to represent individual clay platelets. Some of the studies focused on the geometrical constraints of packing platelets and used successive deposition of particles under gravitational load to

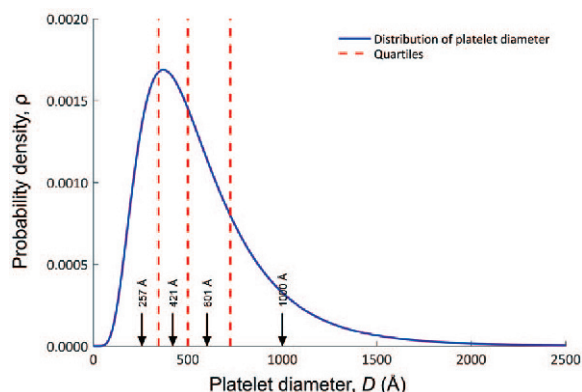* E-mail address of corresponding author:
pellenq@mit.edu

Figure 1. Assumed log-normal distribution of platelet diameters (mean $\mu = 500$ Å, standard deviation $\sigma = 1.73$ Å). Each quartile is represented by its mean value.

reproduce microstructural arrangement of particles (Coelho *et al.*, 1997; Ferrage *et al.*, 2015). A multiscale approach to understanding the intercalation and mechanical properties in clay-polymer composite materials was introduced by Suter *et al.* (2015). The use of multiscale methods to transfer essential information between scales was proposed by Ebrahimi *et al.* (2014) and Whittle *et al.* (2016).

A mesoscale-modeling approach was described by Ebrahimi *et al.* (2014) to simulate the formation of clay aggregates using the Gay-Berne (GB) potential (Gay and Berne, 1981). The method starts with calculation of the change in free energy as a function of separation distance from atomistic scale models of face-to-face and edge-to-edge interactions between two clay plate-

lets. The specific structure of natural Wyoming Na-montmorillonite used in the full atomistic simulations includes isomorphous substitutions in both tetrahedral and octahedral sheets with the following experimental formula: $Na_{0.75}nH_2O\text{-}[Si_{7.75}Al_{0.25}][Al_{3.5}Mg_{0.5}]O_{20}(OH)_4$. The isomorphous substitutions in Wyoming Na-montmorillonite correspond to a cation exchange capacity (CEC) of 102 meq/100 g. Data from these simulations are then used to calibrate the GB potential that represents each platelet as a single-site ellipsoidal body. The prediction of the model for single size (*i.e.* monodisperse) clay nanoplatelets was validated with nano-indentation results, electron microscopy, and X-ray diffraction experiments. The current study extends previous analyses to study the effects of the heterogeneity of platelet sizes at the mesoscale on the microstructure of the soil, distribution of aggregate sizes, and mechanical properties of the system.

METHODOLOGY

The proposed modeling starts with the assumption of a log-normal distribution for clay platelet sizes with mean $\mu = 500$ Å and standard deviation $\sigma = 1.73$ Å (Figure 1). Mean values of the quartiles were chosen as representative sizes of the distribution ($D = 257, 421, 601$, and 1000 Å). At the mesoscale, each clay layer is represented by an ellipsoidal particle (*i.e.* without detailed atomistic structure) and their interactions modeled using the GB potential (Figure 2) (Gay and Berne, 1981). The screening effect of water molecules and ions on the interaction between clay platelets is captured by the calculated free
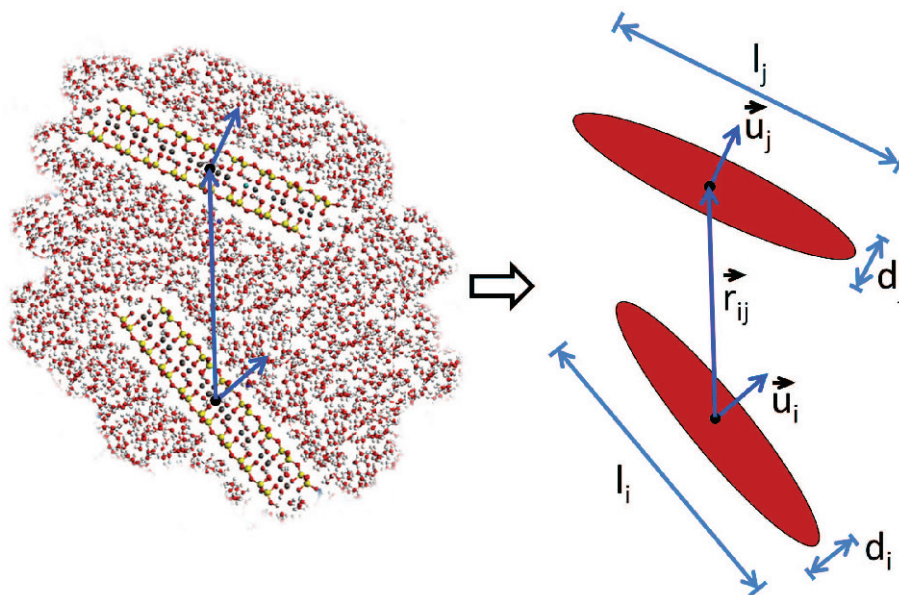

Figure 2. Interactions between two clay platelets are approximated by single-site potential functions for an ellipsoidal body (GB potential).
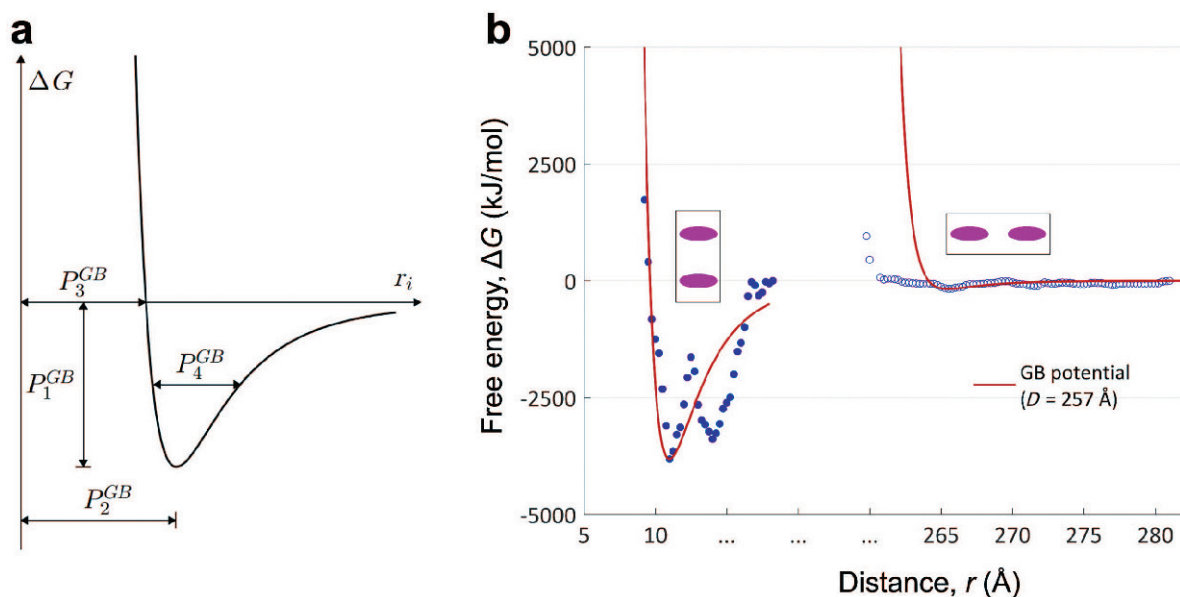
Figure 3. Free energy for interaction of two ellipsoidal clay particles using GB potential: (a) input parameters for GB potential; (b) calibration of parameters for particles with diameter, $D = 257$ Å.

energy. As a result, the computational cost of modeling assemblies of clay platelets to study the formation of clay aggregates is reduced. The GB potential is an anisotropic form of the Lennard Jones potential with potential energy defined by:

$$U = 4\varepsilon \left\{ \left(\frac{\sigma}{h_{12} + \sigma} \right)^{12} - \left(\frac{\sigma}{h_{12} + \sigma} \right)^{6} \right\} \eta_{12} \chi_{12} \quad (1)$$

where $\varepsilon = 1$ determines the energy scale, σ is the atomic interaction radius, and h_{12} is a function that approximates the anisotropic interparticle distance. η_{12} and χ_{12} characterize anisotropic interactions of particles due to their shapes and relative orientations. The GB potential can be defined from four characteristic input parameters (Figure 3a):

    (1) Energy well depth, $P_1 = -\varepsilon\eta_{12}\chi_{12}$
    (2) Separation distance, $P_2 = r - h_{12} + 0.1225\sigma$
    (3) Soft contact distance, $P_3 = r - h_{12}$
    (4) Characteristic well depth, $P_4 = 0.3508\sigma$

where $\mathbf{r_{12}} = \mathbf{r_2} - \mathbf{r_1} = r\,\hat{\mathbf{r}}_{12}$ is the center-to-center separation vector, r is center-to-center distance, $\hat{\mathbf{r}}_{12}$ is the unit vector.

Optimized values of these parameters were obtained through fitting to the face-to-face and edge-to-edge free-energy profiles (Figure 3b for $D = 257$ Å). This was accomplished by minimizing a cost function as described by Ebrahimi *et al.* (2014). Following a similar procedure, the GB potential was calibrated for different platelet sizes (Table 1). The mesoscale simulations are based on the GB potential as implemented (Brown *et al.*, 2009) in the *LAMMPS* code (Plimpton, 1995).

So-called NPT ensembles (where the number of atoms (N), the pressure (P), and the temperature (T), are conserved) were used on four monodisperse systems (with platelet diameters of $D = 257$, 421, 601, or 1000 Å) and one polydisperse system (having 25% of each size) at constant temperature, $T = 300$ K. The total number of platelets in each case was 1000. The pressure was applied as a step function (Figure 4) with different simulation timescales for different confining pressures (Table 2). All samples were equilibrated initially at $P = 1$ atm. The Nosé–Hoover thermostat (Nosé, 1984; Hoover, 1985) was used to control temperature and the Parrinello–Rahman barostat (Parrinello and Rahman,

Table 1. Parameter values of the GB potential for different platelet diameters, D.

D (Å)	GB calibration case			
	257	421	601	1000
2a, 2b (Å)	261.12	425.12	605.12	1004.12
2c (Å)	9.62	9.62	9.62	9.62
σ (Å)	11.00	11.00	11.00	11.00
ε_a, ε_b	12.77	12.86	12.90	12.94
ε_c	281.17	463.84	664.26	1108.46

Table 2. Time length of simulations performed in NPT (T = 300 K) ensemble for different confining pressure, P_1, t_1, t_f (Figure 4).

P_1 (atm)	P_0 = 0 atm	P_0 = 1 atm			
	1	10	50	300	800
t_1 (ns)	40	120	120	120	120
t_f (ns)	1200	360	320	240	200

1981) to control pressure in the system. The pressure- and temperature-damping parameters were 1 ns and 0.001 ns, respectively. The equations of motion were integrated with an integration time step of 40 fs (femtosecond). Ten different simulations were conducted at each selected pressure, assuming random orientations of 1000 platelets within a defined cubic space and an initial spacing, r_a, larger than the diameter of the largest platelet (r_a = d_{max}+ 20 Å). Periodic boundary conditions were applied to all systems. The average properties of the final states are reported.

Mechanical properties were reported based on use of a quasi-static method to construct stress-strain curves (Aghaei *et al.*, 2009) and calculating elastic stiffness values in the small-strain regime. The algorithm consists of two steps: (1) application of a small homogeneous strain to the system; and (2) relaxing the strain step over a time period using an NVT ensemble (*i.e.* simulations in which the number of atoms (N), volume (V), and temperature (T) of the system are conserved) at T = 0.01 K. Components of the stress tensor are determined by averaging over the last 10% of the relaxation time period (simulation details in Table 3).

The proposed method is based on the assumption of rigid platelets. The charge distributions and the existence of local defects associated with isomorphous substitutions at the atomistic scale are modeled precisely at pH = 7. As a result, the coarse-grained model allows relevant system sizes and timescales to be accessed to simulate the formation of clay aggregates. As will be discussed, the current model provides acceptable first-order comparison with experiments based on the microporosity. The effect of change in the charge distribution due to change in the pH and the elasticity of individual clay platelets are beyond the scope of the present study and could be examined in future research.

RESULTS AND DISCUSSION

The system of rigid ellipsoids in an NPT ensemble (T = 300 K) under confining pressure evolving toward a final "jamming state" configuration which is characterized by no further change in the potential energy of the system was described by Ebrahimi *et al.* (2014). In the typical final 'jammed states' of the systems at different confining pressures for the case of monodisperse particles with D = 601 Å (Figure 5), platelets are color coded based on the orientation of their normal vector with respect to the Z axis (β angle). The *QMGA* software (Gabriel *et al.*, 2008) was used for graphical visualization of the system. As the confining pressure increased, more platelets clustered to form aggregates which share approximately the same orientation. As a result, the color spectrum decreased with increasing confining pressure. At the highest pressure (here P = 800 atm) platelets started to slide against each other (Figure 5d). As the platelet diameter increased, the final state of the particle assemblages showed larger aggregate sizes and less diversity in platelet orientation (Figure 6). In simulations with polydisperse particles (Figure 7a,b, the results are
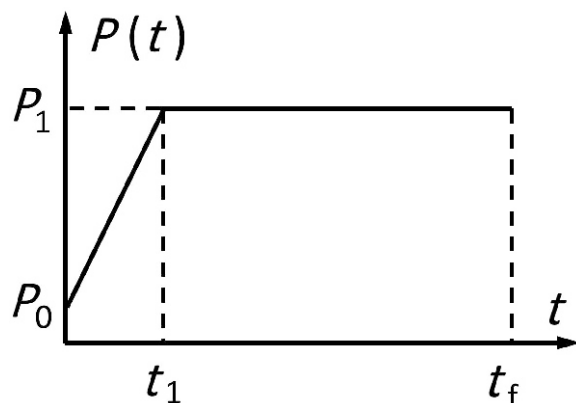
Figure 4. Step function of applied pressure, $P(t)$, in NPT simulations.

Table 3. Details of the simulations used to calculate the elastic properties.

D (Å)	257 or 421 or 601 Four sizes (including 1000)	1000
dt (fs)	5	5
d_ε	2.5×10^{-5}	5×10^{-5}
n_s	12	50
t_r (ps)	1000	100
t_s (ps)	100	10

dt: time step, d_ε: strain step, n_s: number of steps, t_r and t_s: relaxation time and sampling period for each strain step, D: diameter of the platelet.

Figure 5. Examples of the final configuration of the system of particles with diameter $D = 601$ Å at pressure $P = $ (a) 1 atm; (b) 10 atm; (c) 300 atm; and (d) 800 atm. The orientations of the particles are color coded according to the β angle, the orientation of their normal vector with respect to the Z axis (colorbar A). By increasing the pressure the spectrum of colors decreased as the stack size increased and the system became more ordered. At high pressure ($P = 800$ atm), platelets started to slide against each other.

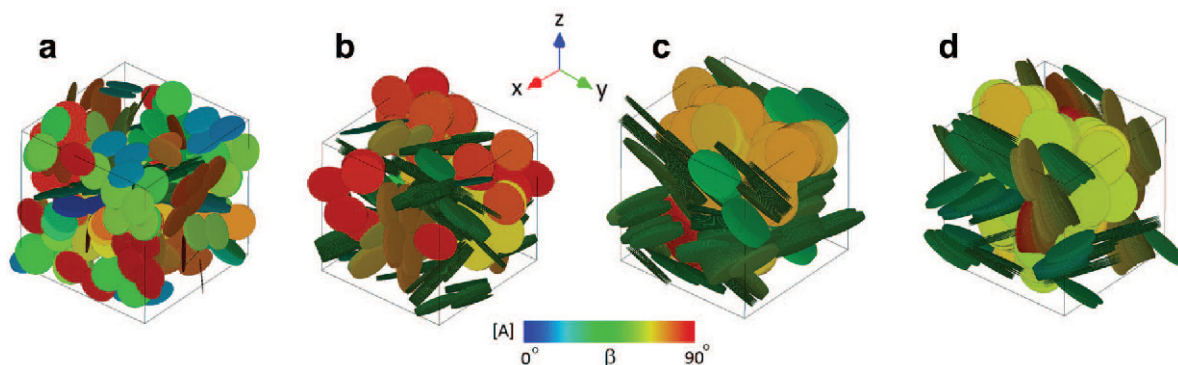color coded based on the size of individual platelets), increases in pressure from $P = 1$ atm (Figure 7c) to 800 atm (Figure 7d) resulted in more ordered systems (in Figure 7c and d the platelets are color coded based on their orientations which shows a more uniform color at higher pressure). In the following sections, the geometrical and mechanical properties of the system are analyzed to quantify the qualitative descriptions above and identify important parameters that affect the microstructure and stiffness of the clay aggregates.

Microstructure

The following four criteria adopted from Chen *et al.* (2013) are used to determine whether two platelets form part of a clay aggregate (Figure 8):

(1) The absolute value of a scalar product of the two normal vectors of the platelets is >0.95 ($|n1{\cdot}n2| > 0.95$).

(2) Their distance is less than an upper limit, r_1, which depends on the type of platelets. If platelet 1 has a diameter D_1 and platelet 2 has a diameter D_2, $r_1 = |D_1 - D_2|/2$.

(3) The distance in the direction of the normal vector of platelet 1 (n_1) is $< r_2$.

(4) The distance in the direction of normal vector of platelet 2 (n_2) is $< r_2$.

The current analysis assumes that r_2 is 25% larger than the equilibrium distance for face-to-face interactions (11 Å, see Ebrahimi *et al.* (2014)) so $r_2 = 13.75$ Å.

The distribution of aggregate stack sizes for each of the ten samples associated with each simulated pressure is fitted to a lognormal distribution function and averaged to report mean and standard deviation of stack size (after Ebrahimi *et al.*, 2014). The results of the geometrical analysis of the aggregates (Figure 9) showed that by increasing platelet size from $D = 257$ Å to $D = 1000$ Å, the average number of platelets per aggregate increased because larger platelets can interact with larger numbers of neighboring platelets as interactions scale with their surface area. Increasing the confining pressure from 1 atm also increased the size of the aggregate stacks, with maximum thickness occurring at pressures ranging from 50 atm at $D = 1000$ Å to 300 atm for $D = 257$ Å.

Further increases in the confining pressure led to a decrease in aggregate size because platelets started to slide against each other and their distance became larger
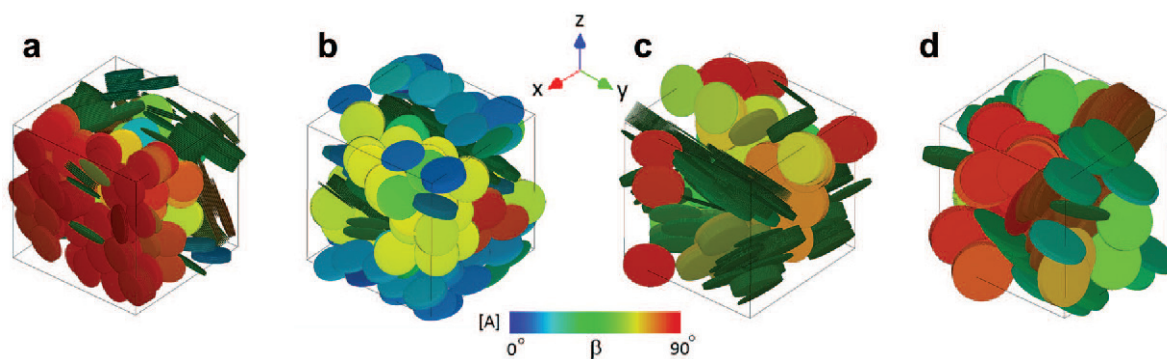
Figure 6. Examples of the final configuration of the system of particles with diameter D at pressure $P = 50$ atm: (a) $D = 257$ Å; (b) $D = 421$ Å; (c) $D = 601$ Å; and (d) $D = 1000$ Å. The orientations of the particles are color coded according to the β angle, the orientation of their normal vector with respect to the Z axis (colorbar A). By increasing the diameter, the average stack size increased.
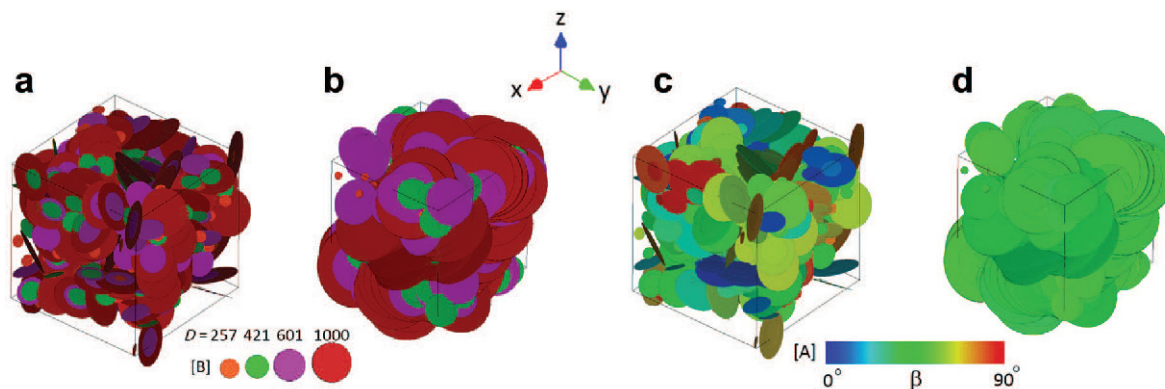
Figure 7. Examples of the final configuration of the polydisperse system of particles with diameters $D = 257, 421, 601$, and 1000 Å at pressure P, (a, c) = 1 atm, (b, d) = 800 atm. In parts a and b, particles are color coded based on their size (colorbar B) and in parts c and d they are color coded according to the β angle, the orientation of their normal vector with respect to the Z axis (colorbar A). By increasing the pressure, the spectrum of color decreases as the system becomes more ordered (see c and d).

than r_1 or r_2. Results from the polydisperse simulations showed an average value of about two platelets per aggregate with negligible change with confining pressure. The average number of platelets per aggregate for different types of Na-smectites (*e.g.* natural samples of montmorillonites, beidellites, nontronites, and hectorite with Na^+ counter ions collected from different areas) has been measured to be between 3 and 10 using transmission electron microscopy, scanning electron microscopy, small angle X-ray scattering, and X-ray diffraction experiments (Pons *et al.*, 1981; Tessier and Pedro, 1981; Rhaiem, 1985; Mystkowski *et al.*, 2000). Values from numerical simulations of monodisperse systems agree well with experimental measurements. In particular, systems with the largest platelet size ($D = 1000$ Å) show aggregate sizes in the range of 5 to 8, while aggregate size in the polydisperse systems are outside this measured range. While increases in pressure in the polydisperse system bring platelets close to each other (similar to the monodisperse cases), their relative displacements are larger than r_1 or r_2, and do not lead to increases in stack size. The current simulations clearly do not represent the size of the natural platelets of montmorillonites but provide a first-order comparison based on micro-porosity. The largest dimension of clay platelet used in the simulation was 1000 Å which is at least ten times smaller than the nanoplatelets found in nature. The results show trends as the platelet size changes, however, and, as will be shown, the resultant

microstructure could capture the overall change trend in the nano-indentation modulus and in the orientation of platelets as confining pressure changes. Better agreement of the results for the system with the largest diameter ($D = 1000$ Å) implies that the distribution of the platelet size in natural Na-smectite (formed naturally in the environment) is oriented toward the larger size.

The degree of orientation of aggregates can be measured using a scalar order parameter, S, where:

$$S = \left\langle \frac{3\cos^2\theta - 1}{2} \right\rangle \qquad (2)$$

where θ is the angle between the normal vector of a platelet and the director of the system (*i.e.* a measure of the average orientation of all the particles in the system). The brackets denote an average over all the particles. For a completely isotropic and randomly oriented system $S = 0$, while perfectly aligned systems have $S = 1$.

The order parameter of monodisperse systems increases with confining pressure and platelet diameter (Figure 10). Systems with smaller platelets have more diverse orientations because they have more freedom to explore the space due to their size. This agrees with experiments (Hetzel *et al.*, 1994) which showed that a more ordered system evolved as lateral extension of the platelets increased. The results (Figure 10) also show that a maximum order parameter occurs at pressures ranging from 50 atm ($D = 1000$ Å) to 300 atm
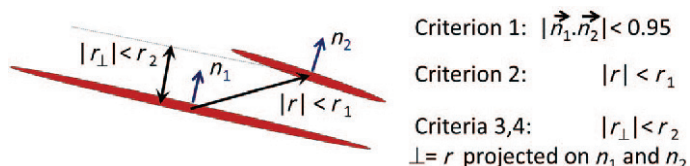

Figure 8. Criteria used for the analysis of aggregation. All of the criteria should be satisfied in order to assign two platelets to a single aggregate.
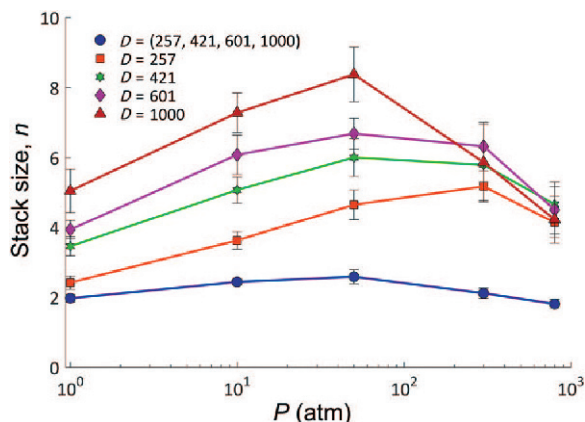
Figure 9. By increasing the pressure on the system, the stack size (*i.e.* the mean size of the clay clusters) increases up to a maximum pressure. Further increase in the pressure resulted in a decrease in the stack sizes due to sliding of the platelets against each other. As the size of the platelet on the monodisperse simulation increased, the size of the clusters increased because of the stronger interaction among platelets with larger surface areas. The polydisperse system showed a smaller stack size (~2).
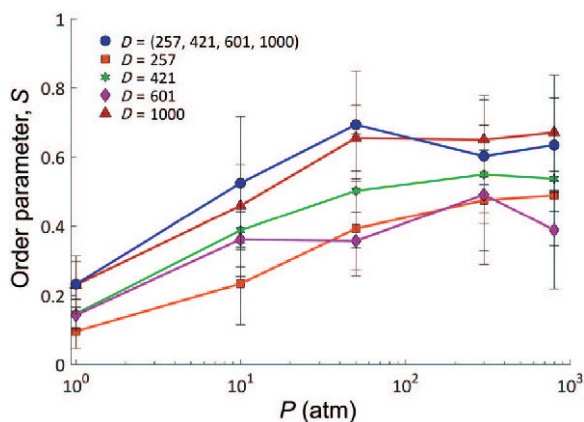
Figure 10. By increasing the pressure, the system became more ordered until reaching a maximum ordered state. Further increase of the pressure resulted in almost no change in the order parameter because the orientation of platelets remained constant as they started to slide against each other. The monodisperse system with the largest diameter ($D = 1000$ Å) and polydisperse system showed identical ordering with the largest value among all simulated systems.

($D = 257$ Å), *i.e.* greater pressures are needed to achieve ordering with systems consisting of smaller particles. The polydisperse systems exhibit order properties similar to the monodisperse systems where $D = 1000$ Å, suggesting that ordering of the system is influenced by the largest platelets. This result confirms Onsager's (1949) theory which states that by increasing concentration (here equivalent to increasing pressure) a transition occurs from the isotropic phase toward the nematic phase. Moreover, the experimental values of order parameter (Perdigon-Aller *et al.*, 2005) and simulation results as a function of packing density, $\eta = 1-$porosity, are summarized and compared (Figure 11).

The experimental data were obtained for a polydisperse powder of kaolinite particles under different degrees of compaction. Despite the difference in mineralogy between kaolinite and Na-smectite, the values of the order parameters from experiment are on the same order of the simulation results and the change follows the same trend as that of the simulation with polydisperse distribution of particles (circles in Figure 11).

The compression behavior of the mesoscale particle assemblies in ϕ-log P (*i.e.* porosity-log pressure) space (Figure 12) shows that the experimental results for Na-smectite samples (Mesri and Olson, 1971; Börgesson *et al.*, 1988; Marcial *et al.*, 2002; Likos and Lu, 2006) are
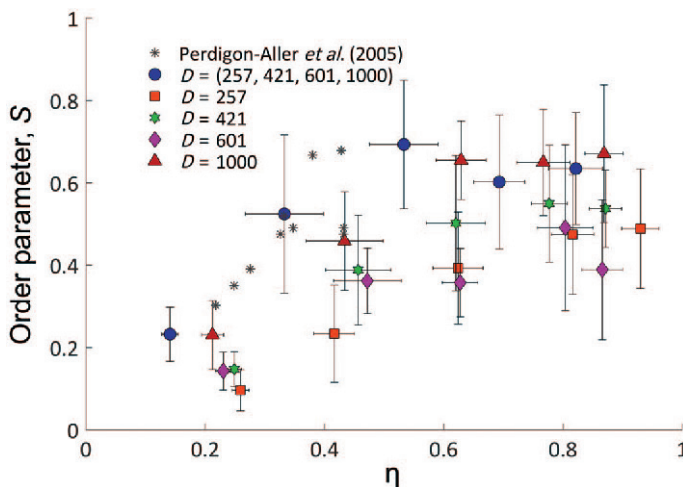
Figure 11. Variation of order parameter with clay packing density, η (1−porosity). Experimental data for natural kaolinite powder were taken from Perdigon-Aller *et al.* (2005). The results of the polydisperse simulations (circles) follow the experimental trend of polydisperse kaolinite particles under different degrees of compaction.

Figure 12. Slope of the compression curves from simulations and experiments. Experimental data for Na-smectites were taken from Mesri and Olson (1971), Börgesson *et al.* (1988), Marcial *et al.* (2002), and Likos and Lu (2006) (assuming $K_0 = 0.5$ to calculate the confining pressure). Casey (2014) reported some triaxial compression tests on Gulf of Mexico (GoM(EI)) and London clay up to high stress with continuous measurement of K_0 values.
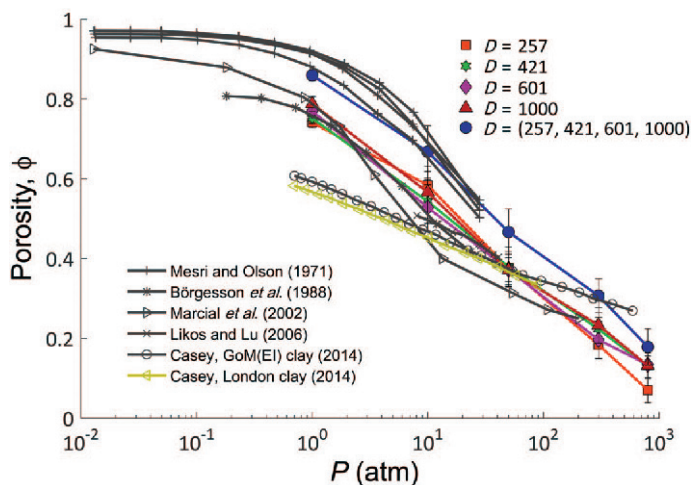
in close agreement with the simulations in the virgin compression region. More recent experimental results (Casey, 2014), however, showed a smaller slope over the wide range of pressure compared to simulated values. This difference can be explained by the mineralogy of the soil samples in the latter experiment. In both types of samples in Casey (2014) (GoM(EI) and London clay), only ~50% of the soil was clay (and was a mixture of illite-smectite; ilite is stiffer than smectite). The rest of

the soil in both cases consisted of silt and sand which are stiffer than clay. As a result, the mixture shows less compressibility than the simulations and other experiments (on Na-smectite).

Mechanical properties

The mean and standard deviation of the elastic constants at each pressure for each of the monodisperse and the polydisperse systems were calculated from the ten

Table 4. Elastic constant properties (GPa) calculated for $D = 257$ Å platelets at different confining pressure, P. The $<\cdot>$ symbol denotes the average of the property (in bold).

P (atm)	— 1 —		— 10 —		— 50 —		— 300 —		— 800 —	
	$<\cdot>$	±	$<\cdot>$	±	$<\cdot>$	±	$<\cdot>$	±	$<\cdot>$	±
C_{11}	**0.36**	0.08	**0.57**	0.12	**1.21**	0.28	**2.75**	0.70	**5.75**	1.82
C_{22}	**0.37**	0.07	**0.60**	0.16	**1.18**	0.23	**3.03**	0.95	**5.76**	1.29
C_{33}	**0.34**	0.03	**0.51**	0.11	**1.02**	0.24	**2.92**	0.88	**5.22**	1.35
C_{44}	**0.10**	0.02	**0.18**	0.09	**0.28**	0.14	**0.55**	0.39	**1.32**	0.75
C_{55}	**0.08**	0.03	**0.16**	0.05	**0.28**	0.07	**0.48**	0.16	**1.27**	0.42
C_{66}	**0.10**	0.03	**0.17**	0.08	**0.36**	0.20	**0.52**	0.23	**1.76**	0.58
C_{12}	**0.11**	0.04	**0.15**	0.08	**0.46**	0.07	**1.56**	0.40	**3.55**	0.66
C_{13}	**0.09**	0.03	**0.16**	0.05	**0.43**	0.11	**1.57**	0.29	**3.49**	0.38
C_{14}	**−0.02**	0.03	**−0.02**	0.08	**−0.03**	0.11	**−0.01**	0.16	**−0.07**	0.39
C_{15}	**−0.04**	0.03	**−0.04**	0.06	**0.00**	0.13	**−0.10**	0.22	**−0.36**	0.63
C_{16}	**−0.02**	0.03	**−0.03**	0.04	**0.00**	0.12	**0.06**	0.16	**0.04**	0.54
C_{23}	**0.10**	0.02	**0.14**	0.07	**0.44**	0.08	**1.54**	0.34	**3.46**	0.28
C_{24}	**−0.02**	0.03	**−0.06**	0.06	**−0.04**	0.12	**−0.07**	0.22	**−0.13**	0.39
C_{25}	**−0.03**	0.02	**−0.06**	0.07	**−0.04**	0.06	**−0.05**	0.13	**−0.17**	0.49
C_{26}	**−0.02**	0.03	**−0.05**	0.05	**−0.04**	0.12	**−0.06**	0.24	**−0.05**	0.51
C_{34}	**−0.03**	0.04	**−0.06**	0.06	**−0.10**	0.09	**−0.07**	0.20	**−0.29**	0.41
C_{35}	**−0.03**	0.02	**−0.05**	0.08	**−0.04**	0.09	**−0.08**	0.17	**−0.42**	0.93
C_{36}	**−0.03**	0.02	**−0.06**	0.06	**−0.07**	0.12	**−0.04**	0.15	**−0.03**	0.30
C_{45}	**0.00**	0.03	**0.00**	0.04	**−0.03**	0.07	**−0.05**	0.11	**0.05**	0.28
C_{46}	**0.00**	0.02	**−0.01**	0.04	**0.00**	0.12	**−0.04**	0.17	**0.01**	0.36
C_{56}	**0.00**	0.02	**−0.01**	0.05	**0.02**	0.09	**−0.06**	0.14	**0.03**	0.32

Table 5. Elastic constant properties (in GPa) calculated for $D = 421$ Å platelets at different confining pressure, P. The $<\cdot>$ symbol denotes the average of the property (in bold).

P (atm)	— 1 —		— 10 —		— 50 —		— 300 —		— 800 —	
	$<\cdot>$	±	$<\cdot>$	±	$<\cdot>$	±	$<\cdot>$	±	$<\cdot>$	±
C_{11}	**0.41**	0.07	**0.94**	0.39	**1.55**	0.36	**4.03**	0.90	**6.65**	1.90
C_{22}	**0.42**	0.06	**0.89**	0.32	**1.59**	0.33	**3.84**	0.75	**7.09**	0.93
C_{33}	**0.36**	0.07	**0.70**	0.21	**1.40**	0.45	**3.15**	0.95	**5.83**	1.30
C_{44}	**0.09**	0.02	**0.24**	0.06	**0.46**	0.18	**0.68**	0.22	**1.44**	0.43
C_{55}	**0.09**	0.02	**0.19**	0.05	**0.41**	0.18	**0.71**	0.18	**1.17**	0.38
C_{66}	**0.10**	0.04	**0.30**	0.16	**0.47**	0.17	**0.95**	0.38	**1.54**	0.55
C_{12}	**0.13**	0.03	**0.27**	0.10	**0.61**	0.10	**1.92**	0.31	**4.24**	0.69
C_{13}	**0.12**	0.03	**0.23**	0.05	**0.56**	0.12	**1.77**	0.22	**3.72**	0.48
C_{14}	**−0.01**	0.03	**0.00**	0.05	**−0.05**	0.09	**0.00**	0.18	**−0.01**	0.36
C_{15}	**−0.01**	0.02	**−0.02**	0.07	**−0.07**	0.23	**−0.01**	0.45	**0.07**	0.77
C_{16}	**−0.01**	0.02	**0.00**	0.06	**−0.03**	0.23	**−0.05**	0.39	**−0.22**	0.84
C_{23}	**0.11**	0.03	**0.25**	0.06	**0.59**	0.11	**1.76**	0.24	**3.94**	0.35
C_{24}	**−0.02**	0.02	**−0.03**	0.06	**0.03**	0.18	**−0.05**	0.39	**0.10**	0.70
C_{25}	**−0.02**	0.02	**−0.02**	0.03	**−0.01**	0.11	**−0.07**	0.18	**−0.03**	0.47
C_{26}	**−0.02**	0.03	**−0.03**	0.07	**−0.05**	0.21	**−0.15**	0.34	**−0.29**	0.74
C_{34}	**−0.02**	0.02	**0.00**	0.06	**−0.02**	0.15	**−0.09**	0.30	**−0.06**	0.77
C_{35}	**−0.02**	0.02	**−0.01**	0.05	**−0.07**	0.20	**−0.02**	0.43	**−0.02**	0.70
C_{36}	**−0.02**	0.02	**0.00**	0.06	**−0.04**	0.06	**−0.04**	0.08	**−0.08**	0.36
C_{45}	**0.00**	0.02	**0.01**	0.06	**0.03**	0.10	**−0.06**	0.12	**−0.07**	0.31
C_{46}	**−0.01**	0.02	**0.02**	0.05	**0.03**	0.05	**−0.01**	0.15	**−0.07**	0.34
C_{56}	**0.00**	0.02	**0.01**	0.05	**0.00**	0.12	**0.04**	0.26	**0.03**	0.42

samples associated with each simulated system (Tables 4−8). The results suggest cubic symmetry for the elastic constants with three independent elastic stiffness values: C_{11} (longitudinal constant), C_{12} (off diagonal constant), and C_{44} (shear constant). They all increased by increasing confining pressure in all cases which could be explained by decreasing porosity of the samples. Mechanical properties were validated by calculating the indentation

Table 6. Elastic constant properties (in GPa) calculated for $D = 601$ Å platelets at different confining pressure, P. $<\cdot>$ symbol denotes average of the property (bold face).

P (atm)	— 1 —		— 10 —		— 50 —		— 300 —		— 800 —	
	$<\cdot>$	±	$<\cdot>$	±	$<\cdot>$	±	$<\cdot>$	±	$<\cdot>$	±
C_{11}	**0.45**	0.04	**1.09**	0.14	**1.86**	0.21	**5.63**	2.06	**7.85**	1.93
C_{22}	**0.48**	0.04	**1.39**	0.56	**2.36**	0.51	**4.98**	1.53	**8.17**	1.83
C_{33}	**0.37**	0.05	**0.94**	0.08	**1.74**	0.37	**4.86**	1.73	**8.89**	2.54
C_{44}	**0.09**	0.01	**0.27**	0.10	**0.50**	0.11	**0.98**	0.26	**2.08**	0.74
C_{55}	**0.08**	0.04	**0.29**	0.05	**0.42**	0.17	**1.41**	0.46	**1.81**	0.78
C_{66}	**0.11**	0.01	**0.36**	0.13	**0.48**	0.08	**1.09**	0.64	**1.74**	0.52
C_{12}	**0.14**	0.01	**0.33**	0.08	**0.70**	0.05	**2.15**	0.50	**4.10**	0.40
C_{13}	**0.11**	0.02	**0.29**	0.03	**0.72**	0.09	**2.48**	0.36	**4.19**	0.61
C_{14}	**0.00**	0.01	**0.01**	0.06	**0.01**	0.07	**−0.03**	0.15	**0.26**	0.23
C_{15}	**−0.04**	0.01	**0.03**	0.10	**−0.05**	0.21	**0.20**	1.24	**−0.10**	0.90
C_{16}	**−0.01**	0.03	**0.01**	0.03	**0.00**	0.10	**−0.26**	0.36	**0.46**	0.44
C_{23}	**0.12**	0.01	**0.36**	0.11	**0.76**	0.11	**2.05**	0.28	**4.42**	0.56
C_{24}	**0.01**	0.02	**−0.01**	0.07	**−0.11**	0.20	**0.02**	0.28	**0.64**	0.39
C_{25}	**−0.02**	0.02	**0.02**	0.06	**−0.04**	0.07	**−0.14**	0.26	**−0.17**	0.31
C_{26}	**0.01**	0.03	**−0.01**	0.06	**−0.05**	0.07	**−0.17**	0.33	**0.25**	0.21
C_{34}	**0.00**	0.01	**−0.03**	0.08	**0.00**	0.06	**0.07**	0.24	**−0.20**	0.93
C_{35}	**−0.04**	0.01	**0.01**	0.08	**−0.15**	0.08	**−0.03**	0.29	**−0.44**	0.26
C_{36}	**0.00**	0.01	**0.01**	0.03	**−0.04**	0.08	**−0.18**	0.21	**0.13**	0.15
C_{45}	**0.00**	0.01	**−0.02**	0.01	**−0.01**	0.07	**−0.16**	0.25	**0.10**	0.23
C_{46}	**0.00**	0.01	**−0.03**	0.02	**0.02**	0.05	**−0.23**	0.27	**−0.16**	0.24
C_{56}	**0.00**	0.01	**0.10**	0.10	**0.03**	0.07	**0.03**	0.14	**0.40**	0.35

Table 7. Elastic constant properties (GPa) calculated for $D = 1000$ Å platelets at different confining pressure, P. The $\langle \cdot \rangle$ symbol denotes average of the property (bold face).

P (atm)	— 1 —		— 10 —		— 50 —		— 300 —		— 800 —	
	$\langle \cdot \rangle$	±	$\langle \cdot \rangle$	±	$\langle \cdot \rangle$	±	$\langle \cdot \rangle$	±	$\langle \cdot \rangle$	±
C_{11}	**0.96**	0.19	**3.58**	0.95	**5.69**	1.58	**12.89**	5.51	**26.00**	13.30
C_{22}	**1.07**	0.39	**4.02**	1.15	**7.42**	3.33	**15.37**	6.06	**33.47**	15.57
C_{33}	**0.92**	0.13	**4.59**	2.37	**6.15**	1.93	**14.24**	5.19	**28.02**	11.90
C_{44}	**0.09**	0.06	**0.42**	0.29	**0.75**	0.42	**2.06**	1.26	**5.22**	2.85
C_{55}	**0.07**	0.03	**0.46**	0.28	**0.54**	0.31	**1.53**	0.94	**4.20**	2.72
C_{66}	**0.09**	0.05	**0.43**	0.12	**0.70**	0.58	**2.13**	1.48	**4.62**	2.14
C_{12}	**0.14**	0.07	**0.49**	0.45	**1.36**	0.72	**4.24**	1.45	**8.60**	2.54
C_{13}	**0.13**	0.06	**0.57**	0.61	**0.97**	0.56	**3.75**	1.02	**8.46**	2.81
C_{14}	**0.01**	0.03	**−0.02**	0.18	**−0.03**	0.25	**0.20**	0.47	**−0.49**	1.32
C_{15}	**0.04**	0.09	**0.18**	0.62	**0.43**	0.57	**−0.01**	1.73	**−0.18**	4.21
C_{16}	**0.03**	0.06	**−0.15**	0.61	**0.19**	0.32	**0.99**	1.07	**1.30**	1.99
C_{23}	**0.16**	0.09	**0.54**	0.42	**1.41**	0.60	**4.37**	1.49	**9.33**	2.97
C_{24}	**0.02**	0.05	**0.33**	0.31	**0.20**	0.23	**0.00**	0.82	**0.18**	3.71
C_{25}	**0.01**	0.05	**−0.03**	0.10	**0.05**	0.42	**−0.13**	1.08	**0.09**	2.78
C_{26}	**0.01**	0.05	**0.14**	0.64	**0.26**	0.46	**0.81**	1.31	**1.53**	2.23
C_{34}	**0.02**	0.07	**−0.15**	0.77	**0.02**	0.57	**0.29**	0.92	**−0.33**	4.45
C_{35}	**0.01**	0.11	**0.11**	0.72	**0.05**	1.19	**−0.12**	1.83	**0.89**	5.18
C_{36}	**0.02**	0.02	**0.00**	0.10	**0.26**	0.29	**0.39**	0.31	**0.54**	0.94
C_{45}	**0.00**	0.03	**0.00**	0.23	**0.11**	0.24	**0.26**	0.42	**0.30**	1.06
C_{46}	**−0.01**	0.08	**−0.01**	0.30	**0.26**	0.78	**−0.05**	0.43	**0.25**	0.78
C_{56}	**−0.01**	0.03	**−0.04**	0.12	**−0.12**	0.21	**0.00**	0.47	**−0.62**	1.51

modulus from the elastic constants (C_{ij}) using the derivation by Delafargue and Ulm (2004) for an orthotropic solid.

The experimental indentation modulus for shale and clay samples (with different volume fractions of inclusions, kaolinite, illite-smectite, and other minerals which were identified as chlorite, glauconite, and biotite) (Bobko and Ulm, 2008) and calculated values from simulations as a function of packing density, η, are summarized and compared in Figure 13. As the platelet

Table 8. Elastic constant properties (GPa) calculated for a polydisperse system with $D = 257, 421, 601$, and 1000 Å platelets at different confining pressure, P. The $\langle \cdot \rangle$ symbol denotes the average of the property (in bold).

| P (atm)	— 1 —		— 10 —		— 50 —		— 300 —		— 800 —	
	$\langle \cdot \rangle$	±	$\langle \cdot \rangle$	±	$\langle \cdot \rangle$	±	$\langle \cdot \rangle$	±	$\langle \cdot \rangle$	±
C_{11}	**0.45**	0.10	**1.19**	0.56	**2.57**	1.03	**6.62**	2.74	**14.98**	7.74
C_{22}	**0.46**	0.06	**1.22**	0.44	**2.58**	1.15	**8.34**	2.43	**13.26**	4.45
C_{33}	**0.41**	0.07	**1.11**	0.37	**2.65**	0.95	**6.73**	1.79	**12.01**	2.88
C_{44}	**0.08**	0.02	**0.24**	0.14	**0.48**	0.22	**1.74**	0.51	**2.85**	0.84
C_{55}	**0.07**	0.03	**0.20**	0.18	**0.52**	0.31	**1.50**	0.48	**3.07**	1.49
C_{66}	**0.08**	0.03	**0.20**	0.10	**0.45**	0.27	**1.51**	0.44	**2.80**	0.91
C_{12}	**0.14**	0.02	**0.33**	0.12	**0.80**	0.26	**3.18**	0.61	**6.07**	1.12
C_{13}	**0.12**	0.02	**0.35**	0.14	**0.93**	0.24	**3.17**	0.53	**6.49**	1.30
C_{14}	**0.00**	0.02	**0.00**	0.03	**0.00**	0.14	**−0.04**	0.21	**−0.16**	0.48
C_{15}	**0.01**	0.03	**−0.03**	0.12	**−0.12**	0.34	**−0.19**	1.30	**−0.32**	2.78
C_{16}	**0.01**	0.02	**0.01**	0.09	**0.10**	0.20	**0.26**	0.67	**0.66**	1.14
C_{23}	**0.13**	0.02	**0.33**	0.09	**0.90**	0.26	**3.30**	0.81	**6.28**	0.73
C_{24}	**0.00**	0.02	**−0.03**	0.06	**−0.07**	0.20	**−0.31**	0.65	**−0.76**	1.13
C_{25}	**0.00**	0.01	**−0.02**	0.08	**−0.10**	0.21	**−0.27**	0.55	**−0.30**	0.73
C_{26}	**0.01**	0.03	**0.00**	0.08	**0.01**	0.19	**0.35**	0.98	**0.55**	1.51
C_{34}	**0.00**	0.03	**−0.02**	0.08	**−0.11**	0.23	**−0.36**	0.44	**−0.71**	0.78
C_{35}	**0.00**	0.02	**−0.05**	0.12	**−0.15**	0.35	**−0.09**	0.14	**−0.37**	1.79
C_{36}	**0.00**	0.01	**0.01**	0.06	**0.04**	0.11	**0.03**	0.30	**0.19**	0.38
C_{45}	**0.00**	0.01	**0.01**	0.05	**0.04**	0.15	**0.11**	0.42	**0.28**	0.48
C_{46}	**0.00**	0.01	**0.03**	0.05	**−0.03**	0.10	**−0.14**	0.32	**−0.21**	0.73
C_{56}	**−0.01**	0.02	**−0.02**	0.10	**−0.04**	0.14	**−0.09**	0.35	**−0.26**	0.43
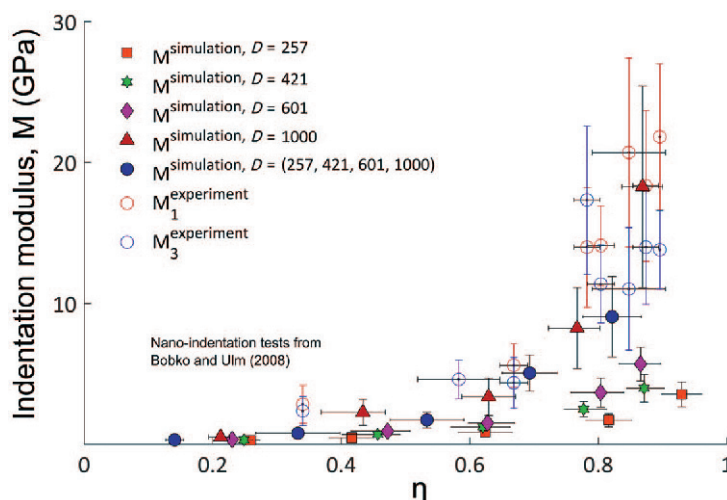
Figure 13. Comparison of indentation modulus *vs.* clay packing density, η (1−porosity) between simulation results (for different platelet diameters and different pressures) and experimental data taken from Bobko and Ulm (2008) . Subscripts 1 and 3 stand for indentation parallel and normal to the bedding plane. Increase of platelet diameter resulted in increase of the indentation modulus. The monodisperse system with the largest platelet diameter ($D = 1000$ Å) and the polydisperse system were used to capture experimental values.

size increased, the indentation modulus increased due to greater interaction between larger platelets. The results of the simulations of the monodisperse system with $D = 1000$ Å and of the polydisperse system follow the experimental trend which suggests that these larger particles are more typical of those found in natural clays.

CONCLUSIONS

The change in free energy between two clay nanoplatelets in the face-to-face and edge-to-edge interaction (previously calculated using full atomistic simulations (Ebrahimi *et al.*, 2014)) was used to calibrate interaction of four different platelet sizes. The calibration of the GB potential approximated each platelet as a single-site rigid ellipsoid. Four monodisperse systems and one polydisperse system were then simulated, each having 1000 platelets at different confining pressures. The mean thickness of the clay aggregates increased with increasing platelet size and the particle assemblies became more ordered. As confining pressure increased, the system followed a similar trend of increase in the order parameter and aggregate size until reaching a pressure limit. Further increases in the confining pressure had no effect on the order parameter but the aggregate thickness decreased due to sliding of platelets against each other. The pressure limit at which the system reached its maximum ordered state decreased as the platelet size increased. The polydisperse simulations generated smaller mean aggregate stacks ($n = 2$) than are typically reported from experiments on natural Na-smectite samples ($3-10$) while monodisperse simulation of platelets with $D = 1000$ Å matched closely the reported stack size of ($n =$

$5-8$) which implies that distribution of platelet sizes in natural samples is oriented toward larger platelets. The monodisperse system with $D = 1000$ Å and the polydisperse system both followed similar changes in ordering of the system as a function of the confining pressure (Figures $9-11$). All of the simulations could predict the slope of the compression curves of natural Na-smectites in the virgin compression region which further validated the proposed mesoscale model (Figure 12). Moreover, the simulations are in good agreement with the experimental indentation modulus which increased with increasing pressure even above the pressure limit for aggregate size and ordering of the system. These results imply an influence by larger platelets on the anisotropy and elastic stiffness parameters of the system (Figure 13). In monodisperse systems, the indentation modulus increased as the platelet size increased due to greater interaction among platelets with larger surface areas.

The current analyses use free energy of interaction between single species of smectite (Wyoming Na-montmorillonite) in liquid water with CEC = 102 meq/100 g. In the future, the influence of platelet charge (amount of isomorphous substitution) and pore-fluid composition (salt concentration, or chemical treatment of pore fluid) on the interaction of platelets (*i.e.* change in the free energy of interaction of platelets) can be studied and implemented in the mesoscale model using a similar multi-scale framework.

REFERENCES

Adams, J.M. (1993) Particle size and shape effects in materials science: examples from polymer and paper systems. *Clay Minerals*, **28**, 509–530.

Aghaei, A., Qomi, M.A., Kazemi, M.T., and Khoei, A.R. (2009) Stability and size-dependency of Cauchy–Born hypothesis in three-dimensional applications. *International Journal of Solids and Structures*, **46**, 1925–1936.

Bobko, C. and Ulm, F.-J. (2008) The nano-mechanical morphology of shale. *Mechanics of Materials*, **40**, 318–337.

Boek, E.S., Coveney, P.V., and Skipper, N.T. (1995) Monte Carlo molecular modeling studies of hydrated Li-, Na-, and K-smectites: Understanding the role of potassium as a clay swelling inhibitor. *Journal of the American Chemical Society*, **117**, 12608–12617.

Börgesson, L., Karnland, O., and Hökmark, H. (1988) *Rheological properties of sodium smectite clay*. SKB, Sweden (http://www.skb.se/publikation/3305/TR88-30webb.pdf).

Boulet, P., Greenwell, H.C., Stackhouse, S., and Coveney, P.V. (2006) Recent advances in understanding the structure and reactivity of clays using electronic structure calculations. *Journal of Molecular Structure: THEOCHEM*, **762**, 33–48.

Brown, W.M., Petersen, M.K., Plimpton, S.J., and Grest, G.S. (2009) Liquid crystal nanodroplets in solution. *The Journal of Chemical Physics*, **130**, 044901.

Carrier, B., Vandamme, M., Pellenq, R.J.-M., and Van Damme, H. (2014) Elastic properties of swelling clay particles at finite temperature upon hydration. *The Journal of Physical Chemistry C*, **118**, 8933–8943.

Casey, B.B.A. (2014) The consolidation and strength behavior of mechanically compressed fine-grained sediments. PhD thesis, Massachusetts Institute of Technology, Massachusetts, USA.

Chen, C.-T., Ball, V., de Almeida Gracio, J.J., Singh, M.K., Toniazzo, V., Ruch, D., and Buehler, M.J. (2013) Self-assembly of tetramers of 5, 6-dihydroxyindole explains the primary physical properties of eumelanin: Experiment, simulation, and design. *ACS Nano*, **7**, 1524–1532.

Coelho, D., Thovert, J.-F., and Adler, P.M. (1997) Geometrical and transport properties of random packings of spheres and aspherical particles. *Physical Review E*, **55**, 1959–1978.

Delafargue, A. and Ulm, F.-J. (2004) Explicit approximations of the indentation modulus of elastically orthotropic solids for conical indenters. *International Journal of Solids and Structures*, **41**, 7351–7360.

Derjaguin, B.V., Landau, L., and others (1941) Theory of the stability of strongly charged lyophobic sols and of the adhesion of strongly charged particles in solutions of electrolytes. *Acta Physico-Chimica URSS*, **14**, 633–662.

Dijkstra, M., Hansen, J.P., and Madden, P.A. (1995) Gelation of a clay colloid suspension. *Physical Review Letters*, **75**, 2236.

Ebrahimi, D., Pellenq, R.J.-M., and Whittle, A.J. (2012) Nanoscale elastic properties of montmorillonite upon water adsorption. *Langmuir*, **28**, 16855–16863.

Ebrahimi, D., Whittle, A.J., and Pellenq, R.J.-M. (2014) Mesoscale properties of clay aggregates from potential of mean force representation of interactions between nano-platelets. *The Journal of Chemical Physics*, **140**, 154309.

Ferrage, E., Hubert, F., Tertre, E., Delville, A., Michot, L.J., and Levitz, P. (2015) Modeling the arrangement of particles in natural swelling-clay porous media using three-dimensional packing of elliptic disks. *Physical Review E*, **91**,

062210.

Gabriel, A.T., Meyer, T., and Germano, G. (2008) Molecular graphics of convex body fluids. *Journal of Chemical Theory and Computation*, **4**, 468–476.

Gay, J.G. and Berne, B.J. (1981) Modification of the overlap potential to mimic a linear site–site potential. *The Journal of Chemical Physics*, **74**, 3316–3319.

Heinz, H., Koerner, H., Anderson, K.L., Vaia, R.A., and Farmer, B.L. (2005) Force field for mica-type silicates and dynamics of octadecylammonium chains grafted to montmorillonite. *Chemistry of Materials*, **17**, 5658–5669.

Hensen, E.J.M., Tambach, T.J., Bliek, A., and Smit, B. (2001) Adsorption isotherms of water in Li-, Na-, and K-montmorillonite by molecular simulation. *The Journal of Chemical Physics*, **115**, 3322–3329.

Hetzel, F., Tessier, D., Jaunet, A.-M., and Doner, H. (1994) The microstructure of three Na^+ smecites: The importance of particle geometry on dehydration and rehydration. *Clays and Clay Minerals*, **42**, 242–248.

Hoover, W.G. (1985) Canonical dynamics: equilibrium phase-space distributions. *Physical Review A*, **31**, 1695.

Israelachvili, J.N. and Pashley, R.M. (1983) Molecular layering of water at surfaces and origin of repulsive hydration forces. *Nature*, **306**, 249–250.

Jardat, M., Dufrêche, J.-F., Marry, V., Rotenberg, B., and Turq, P. (2009) Salt exclusion in charged porous media: a coarse-graining strategy in the case of montmorillonite clays. *Physical Chemistry Chemical Physics*, **11**, 2023–2033.

Kutter, S., Hansen, J.-P., Sprik, M., and Boek, E. (2000) Structure and phase behavior of a model clay dispersion: A molecular-dynamics investigation. *The Journal of Chemical Physics*, **112**, 311–322.

Li, H., Kang, T., Zhang, B., Zhang, J., and Ren, J. (2016) Influence of interlayer cations on structural properties of montmorillonites: A dispersion-corrected density functional theory study. *Computational Materials Science*, **117**, 33–39.

Likos, W.J. and Lu, N. (2006) Pore-scale analysis of bulk volume change from crystalline interlayer swelling in Na^+- and Ca^{2+}-smectite. *Clays and Clay Minerals*, **54**, 515–528.

Marcial, D., Delage, P., and Cui, Y.J. (2002) On the high stress compression of bentonites. *Canadian Geotechnical Journal*, **39**, 812–820.

Mazo, M.A., Manevitch, L.I., Gusarova, E.B., Shamaev, M.Y., Berlin, A.A., Balabaev, N.K., and Rutledge, G.C. (2008a) Molecular dynamics simulation of thermomechanical properties of montmorillonite crystal. 1. Isolated clay nanoplate. *The Journal of Physical Chemistry B*, **112**, 2964–2969.

Mazo, M.A., Manevitch, L.I., Gusarova, E.B., Berlin, A.A., Balabaev, N.K., and Rutledge, G.C. (2008b) Molecular dynamics simulation of thermomechanical properties of montmorillonite crystal. II. Hydrated montmorillonite crystal. *The Journal of Physical Chemistry C*, **112**, 17056–17062.

Mesri, G. and Olson, R.E. (1971) Consolidation characteristics of montmorillonite. *Géotechnique*, **21**, 341–352.

Murray, H.H. (1991) Overview – clay mineral applications. *Applied Clay Science*, **5**, 379–395.

Mystkowski, K., Środoń, J., and Elsass, F. (2000) Mean thickness and thickness distribution of smectite crystallites. *Clay Minerals*, **35**, 545–557.

Nosé, S. (1984) A unified formulation of the constant temperature molecular dynamics methods. *The Journal of Chemical Physics*, **81**, 511–519.

Onsager, L. (1949) The effects of shape on the interaction of colloidal particles. *Annals of the New York Academy of Sciences*, **51**, 627–659.

Parrinello, M. and Rahman, A. (1981) Polymorphic transitions

in single crystals: A new molecular dynamics method. *Journal of Applied physics*, **52**, 7182−7190.

Pashley, R.M. and Israelachvili, J.N. (1984) Molecular layering of water in thin films between mica surfaces and its relation to hydration forces. *Journal of Colloid and Interface Science*, **101**, 511−523.

Perdigon-Aller, A.C., Aston, M., and Clarke, S.M. (2005) Preferred orientation in filtercakes of kaolinite. *Journal of Colloid and Interface Science*, **290**, 155−165.

Plimpton, S. (1995) Fast parallel algorithms for short-range molecular dynamics. *Journal of Computational Physics*, **117**, 1−19.

Pons, C.H., Tessier, D., Rhaiem, H.B., Tchoubar, D., Van Olphen, H., and Veniale, F., editors (1981) A comparison between X-ray studies and electron microscopy observations of smectite fabric. Pp. 177−185 in: *Proceedings of the International Clay Conference*. Elsevier, Amsterdam.

Rhaiem, B. (1985) Factors affecting the microstructure of smectites−role of cation and history of applied stresses. Pp. 292−297 in: *Proceedings of the International Clay Conference* (C.H. Pons *et al., editors*). Elsevier, Amsterdam.

Sjoblom, K.J. (2015) Coarse-grained molecular dynamics approach to simulating clay behavior. *Journal of Geotechnical and Geoenvironmental Engineering*, 06015013.

Suter, J.L., Coveney, P.V., Greenwell, H.C., and Thyveetil, M.-A. (2007) Large-scale molecular dynamics study of montmorillonite clay: emergence of undulatory fluctuations and determination of material properties. *The Journal of Physical Chemistry C*, **111**, 8248−8259.

Suter, J.L., Groen, D., and Coveney, P.V. (2015) Clay–polymer nanocomposites: Chemically specific multiscale modeling of clay−polymer nanocomposites reveals intercalation dynamics, tactoid self-assembly and emergent materials

properties. *Advanced Materials*, **27**, 957−957.

Tessier, D. and Pedro, G. (1981) Electron microscopy study of Na smectite fabricùrole of layer charge, salt concentration and suction parameters. Pp. 6−12 in: *Proceedings of the International Clay Conference* (C.H. Pons *et al.*, editors). Elsevier, Amsterdam.

Thyveetil, M.-A., Coveney, P.V., Suter, J.L., and Greenwell, H.C. (2007) Emergence of undulations and determination of materials properties in large-scale molecular dynamics simulation of layered double hydroxides. *Chemistry of Materials*, **19**, 5510−5523.

Verwey, E.J.W. and Overbeek, J.T.G. (1999) *Theory of the Stability of Lyophobic Colloids*. Dover Publishing Co., Mineola, New York.

Whitley, H.D. and Smith, D.E. (2004) Free energy, energy, and entropy of swelling in Cs-, Na-, and Sr-montmorillonite clays. *The Journal of Chemical Physics*, **120**, 5387−5395.

Whittle, A.J., Ebrahimi, D., and Pellenq, R.J.-M. (2016) Mesoscale modeling and properties of clay aggregates. Pp. 241−253 in: *Holistic Simulation of Geotechnical Installation Processes* (T. Triantafyllidis, editor). Springer, Berlin.

Young, D.A. and Smith, D.E. (2000) Simulations of clay mineral swelling and hydration: Dependence upon interlayer ion size and charge. *The Journal of Physical Chemistry B*, **104**, 9163−9170.

Zartman, G.D., Liu, H., Akdim, B., Pachter, R., and Heinz, H. (2010) Nanoscale tensile, shear, and failure properties of layered silicates as a function of cation density and stress. *The Journal of Physical Chemistry C*, **114**, 1763−1772.